ACS APPLIED MATERIALS & INTERFACES

Research Article

www.acsami.org

# Corrosion and Tribological Behavior of $ZrO_2$ Films Prepared on Stainless Steel Surface by the Sol–Gel Method

Wei Zhang, Guojun Ji,* Aiming Bu, and Bo Zhang

College of Chemical Engineering, Inner Mongolia University of Technology, Hohhot 010051, China

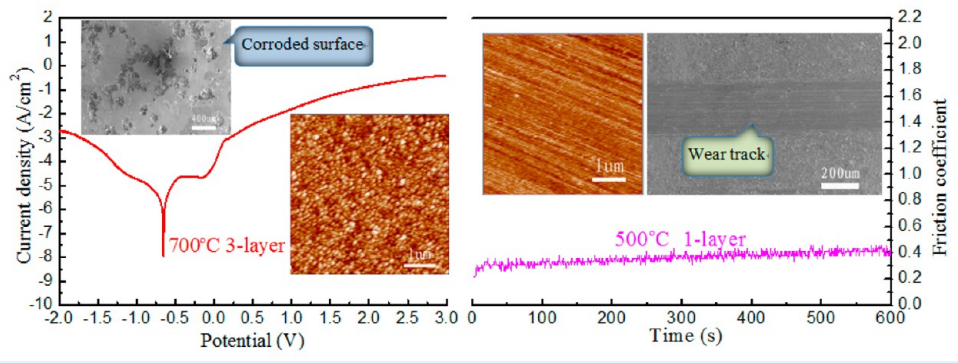


**ABSTRACT:** $ZrO_2$ films with one, two, and three layers were prepared on a 304 stainless steel surface through the sol–gel method, followed by sintering at 500, 600, and 700 °C. The crystal structure and the surface morphology of the films were characterized by X-ray diffraction and atomic force microscopy. The corrosion resistances of uncoated and coated specimens were studied by electrochemical corrosion tests in a 5% NaCl solution at room temperature. The tribological properties of $ZrO_2$ films were investigated using a tribometer. The results showed that the crystal structure of $ZrO_2$ partially transformed from the tetragonal phase to the monoclinic phase with a rise in sintering temperature. The grain size of the $ZrO_2$ films grew, and the surface roughness of the films increased. However, with an increase in the number of film layers, the grain size and the surface roughness of the $ZrO_2$ films decreased and the films became more uniform and denser. $ZrO_2$ films effectively enhanced the corrosion and wear resistances of the stainless steel surface. With the increase of the sintering temperature and the number of layers in the film, the corrosion resistance of the $ZrO_2$ films increased gradually, but the wear resistance of the films slowly decreased. The film with three layers, which was sintered at 700 °C, had the highest corrosion resistance. Nevertheless, the film with one layer, which was sintered at 500 °C, exhibited relatively well wear resistance.

**KEYWORDS:** *$ZrO_2$ films, heat treatment, surface morphology, corrosion, wear*

## 1. INTRODUCTION

Stainless steels have been widely used in various industries because of their good corrosion resistance and mechanical properties. Among of them, 304 austenitic stainless steel is the commonest type of stainless steels. However, due to the low hardness, poor wear resistance of stainless steel, sensitive to pitting corrosion and stress corrosion cracking in chloride solution,[1−3] the strength of the stainless steel can be reduced, which limits its application in industrial production. Therefore, how to improve the corrosion resistance of stainless steel in chloride ion solution and the wear resistance of stainless steel has been a problem. In this case, it came into being and developed rapidly that the ceramic films were used to coat on the stainless steel surface.[4−6]

$ZrO_2$ films possess many excellent physical and chemical properties, such as good light transmission, a high refractive index, a high dielectric constant, a wide band gap, a high melting point, and a low thermal conductivity. In recent years, $ZrO_2$ films have been widely used in industries as a component of optical devices, catalyst supports, oxygen sensors, high-temperature fuel batteries, and semiconductors.[7−12] In addition, $ZrO_2$ films have a high thermal expansion coefficient which is a close match to that of many metals. $ZrO_2$ films also present good chemical stability and high strength, which make them an ideal protective coating against corrosion and wear. At present, the number of investigations on the corrosion and tribological behaviors of $ZrO_2$ films is increasing,[13−21] which have become a new direction of research on surface protection for metal materials.

$ZrO_2$ films can be prepared by various techniques, including chemical vapor deposition,[22] plasma spraying,[23] reactive sputtering,[24] electron beam evaporation,[25] pulsed laser deposition,[26] and sol–gel synthesis.[27] The physical and chemical properties of the $ZrO_2$ films mentioned above strongly depend on the deposition method and the corresponding heat treatment process. Many researches on

Received: August 26, 2015
Accepted: December 7, 2015
Published: December 7, 2015





DOI: 10.1021/acsami.5b07915
ACS Appl. Mater. Interfaces 2015, 7, 28264−28272

**Table 1. Composition of 304 Stainless Steel Substrate**

| element | Fe | C | Cr | Ni | Mn | Si | P | S |
|---|---|---|---|---|---|---|---|---|
| mass percent | ~71 | 0.032 | 18.0 | 8.65 | 1.28 | 0.62 | 0.031 | 0.01 |

the effects of the preparation process on the corrosion and wear properties of $ZrO_2$ films have been done. However, little work on the effect of heat treatment temperature on the structural evaluations, corrosion performance, and tribological properties of $ZrO_2$ sol−gel films on the stainless steel substrate has been reported. These studies can help to optimize the preparation process of the $ZrO_2$ film, as well as improve its physico-chemical properties and service life. Nouri et al.[28] analyzed the effect of the heat treatment process on the corrosion performance of zirconia films produced by the sol−gel dip-coating method on the 316L stainless steel substrates. The results showed that a crystalline tetragonal structure of the films was formed at 700 °C, then transformed to monoclinic phase at 900 °C. The average roughness of the films increased with the rising heat temperature. The films treated at 500 °C had a uniform crack-free structure and the strongest corrosion barrier performance on the 316L stainless steel. Differences in the electrochemical behavior of $ZrO_2$ films at the mentioned temperatures were related to the development of structure and microcracks during the sintering process. Tiwari et al.[29] reported that the defect-free 4 mol % yttria-stabilized zirconia (YSZ) coatings on AISI 316L stainless steel enhanced the pitting potential of the substrate. The tetragonal zirconia structure was obtained at and above 400 °C. Crystallinity and crystallite size were increased and the porosity in the coating was decreased with the increase of the temperature from 400 to 600 °C in heat treatment. The coatings might be useful for implants and surgical instruments to enhance the corrosion and wear resistance.

In this paper, $ZrO_2$ sol−gel films with one, two, and three layers were prepared on the 304 stainless steel substrate surface by a dip-coating technique. The work aims to provide a comprehensive understanding of the effect of sintering temperature and film thickness on the surface morphology, corrosion, and tribological properties of $ZrO_2$ films.

## 2. EXPERIMENTAL SECTION

Tetrabutyl zirconate ($Zr(OC_4H_9)_4$) and absolute ethanol were used as precursor materials. First, tetrabutyl zirconate, absolute ethanol, and acetic acid (volume ratio of 1:4:0.1) were mixed together in a beaker and then vigorously stirred with a magnetic stirrer for 30 min at room temperature. The obtained sol was further aged at room temperature for 24 h. The 304 stainless steel sheets produced by Taiyuan Iron and Steel Group Co., Ltd. were used as substrates. The chemical composition of this material is given in Table 1. Before deposition, substrates were mirror-polished with diamond paste, cleaned in an ultrasonic bath, and rinsed in distilled water. The sol was deposited on the substrates by a dip-coating procedure with a withdrawal speed of 5 mm/min. The film-deposited substrates were dried at 100 °C for 1 h and subsequently sintered, respectively, at 500, 600, and 700 °C for 2 h in air to obtain 1-layer crystallization films. The multilayer films were prepared by repeatedly dip-coating and drying after each deposition. Finally, the films were sintered at different temperatures for 2 h. In addition, the xerogel powder was synthesized by the sol through repeating the above drying−sintering process.

The crystal structures of the $ZrO_2$ xerogel were examined by an X-ray diffraction (XRD) instrument (D/Max-2500, Rigaku) with Cu K$\alpha$ radiation at 40 kV and 120 mA with a 3°/min scanning speed. The thicknesses of the $ZrO_2$ films were measured by an optical profiler (Wyko NT9300, Veeco). The surface morphologies of the samples were observed by an atomic force microscope (AFM) (CSPM4000 SPM, Benyuan) at a scanning rate of 1.0 Hz.

The electrochemical corrosion behaviors of the $ZrO_2$ films were investigated in a 5% NaCl aqueous electrolyte by the potentiodynamic polarization test using an electrochemical workstation (CHI660C, Chenhua). A three-electrode cell was composed of the specimen, which had 1 $cm^2$ exposed areas, as the working electrode; Ag/AgCl as the reference electrode; and Pt as the counter electrode. Electrochemical measurements were carried out at a scan rate of 10 mV/s. The Tafel polarization curves were obtained from −2.0 to 3.0 V. All experiments were conducted at room temperature. Subsequent to the electrochemical measurement, the surface morphologies of corroded specimens were observed with a scanning electron microscope (SEM, S-3400, Hitachi).

The hardnesses of the $ZrO_2$ films were measured by nano-indentation experiments, using a nanoindenter (G200, Agilent) equipped with a Berkovich three-sided diamond tip. The maximum load applied was 5 mN. For each specimen, indentation was conducted at five different points. The tribological properties of the $ZrO_2$ films were evaluated on a ball-on-disk tribometer (CFT-I, Zhongkekaihua) under linear reciprocating sliding conditions. The counterpart was a GCr15 steel ball with a diameter of 3 mm. The friction and wear tests were carried out at an applied load of 0.5 N, a sliding speed of 25 m/s, a one-way sliding distance of 5 mm, and a testing time of 10 min at room temperature. All of the tribological tests were performed at least three times under the same conditions. Afterward, the worn surfaces of the specimens were observed by SEM.

## 3. RESULTS AND DISCUSSION

Figure 1 shows the XRD patterns of the $ZrO_2$ xerogels at room temperature (RT) and those that were sintered at 500, 600, and

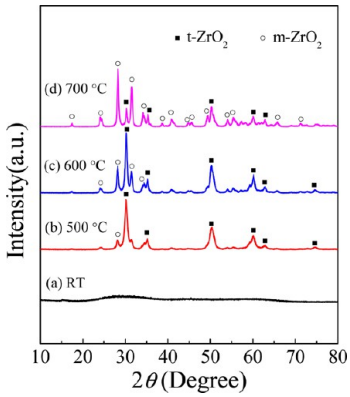


**Figure 1.** XRD patterns of the $ZrO_2$ xerogel at different sintering temperatures.

700 °C for 2 h. As shown in the Figure 1, the $ZrO_2$ xerogels display an amorphous phase at room temperature, and then the $ZrO_2$ is crystallized at high sintering temperature. After sintering at 500 °C, the $ZrO_2$ mainly consists of the tetragonal phase (t-$ZrO_2$) and is accompanied by a small amount of the monoclinic phase (m-$ZrO_2$). When the sintering temperature rises to 600 °C, the t-$ZrO_2$ diffraction peak intensity is enhanced, and the fraction of the m-$ZrO_2$ crystal phase is also increased. However, when the sintering temperature is 700 °C, the intensity of the t-$ZrO_2$ diffraction peaks decreases, and the intensity of the m-$ZrO_2$ peaks clearly increases. This is in good agreement with the published data for the sol−gel derived




DOI: 10.1021/acsami.5b07915
ACS Appl. Mater. Interfaces 2015, 7, 28264−28272

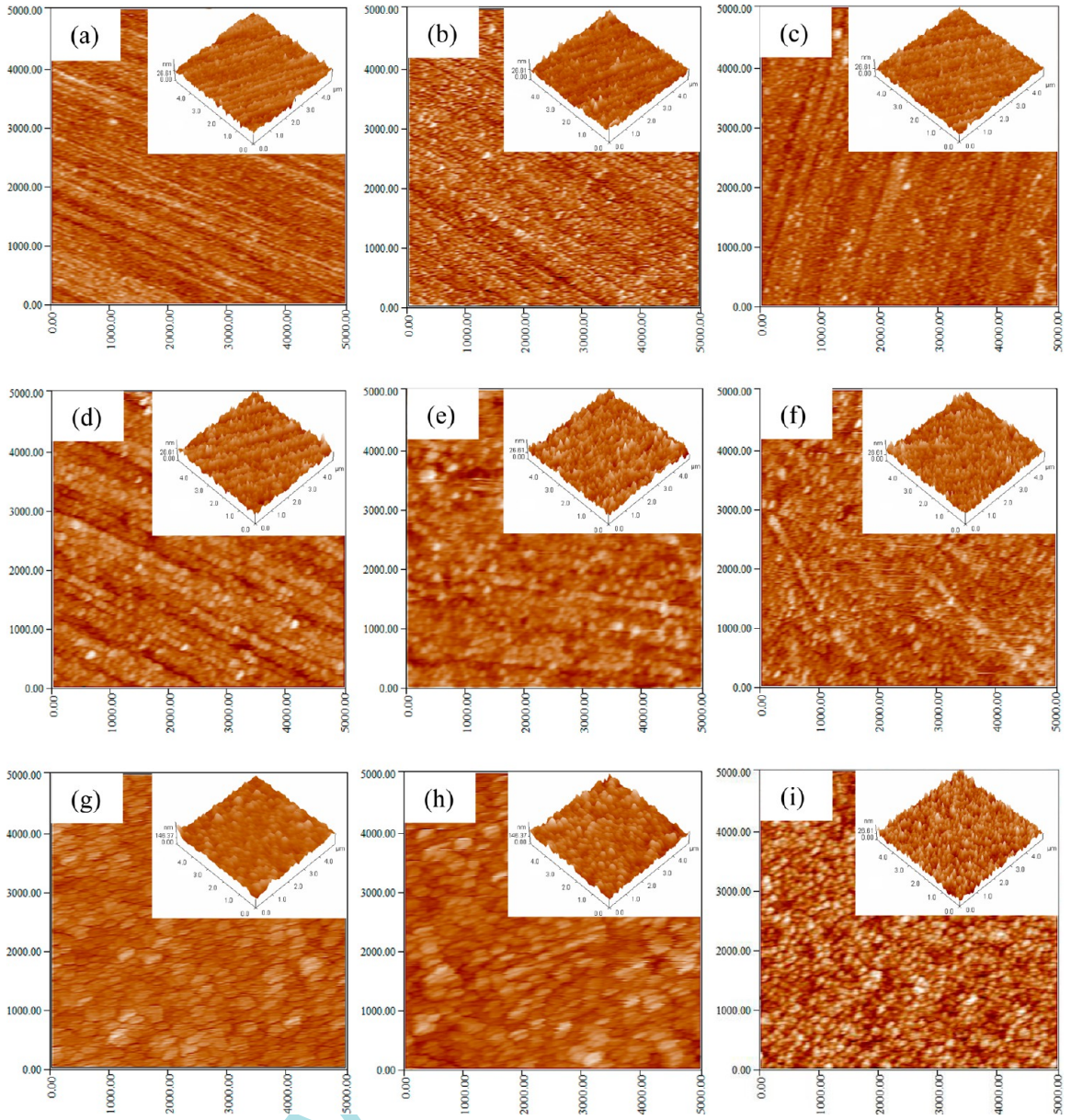


**Figure 2.** AFM images of the $ZrO_2$ films after sintering at different temperatures: (a) 500 °C 1-layer, (b) 500 °C 2-layer, (c) 500 °C 3-layer, (d) 600 °C 1-layer, (e) 600 °C 2-layer, (f) 600 °C 3-layer, (g) 700 °C 1-layer, (h) 700 °C 2-layer, (i) 700 °C 3-layer.

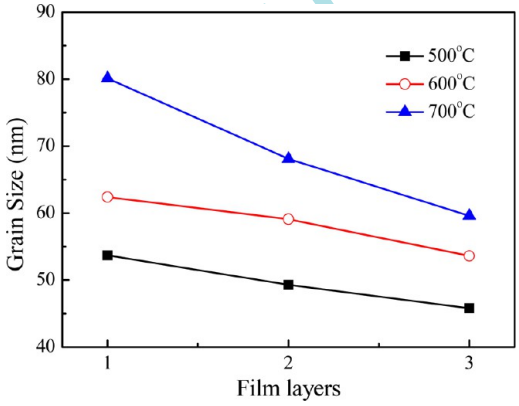


**Figure 3.** Average grain size of the $ZrO_2$ films.

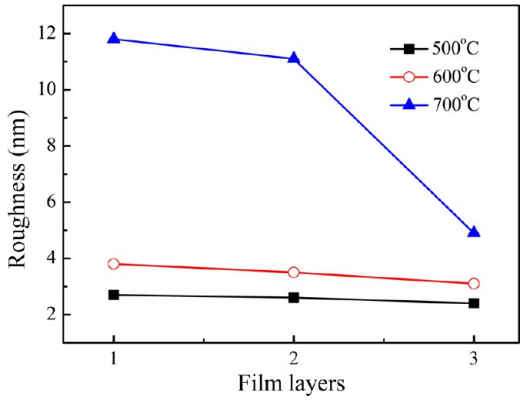


**Figure 4.** Surface roughness of the $ZrO_2$ films.

$ZrO_2$.[30] Meanwhile, with the sintering temperature increasing, the width of diffraction peaks of the tetragonal and monoclinic phases are narrowed, which indicates that the grain size of $ZrO_2$ increased gradually. This can be explained by the growth



DOI: 10.1021/acsami.5b07915
ACS Appl. Mater. Interfaces 2015, 7, 28264−28272

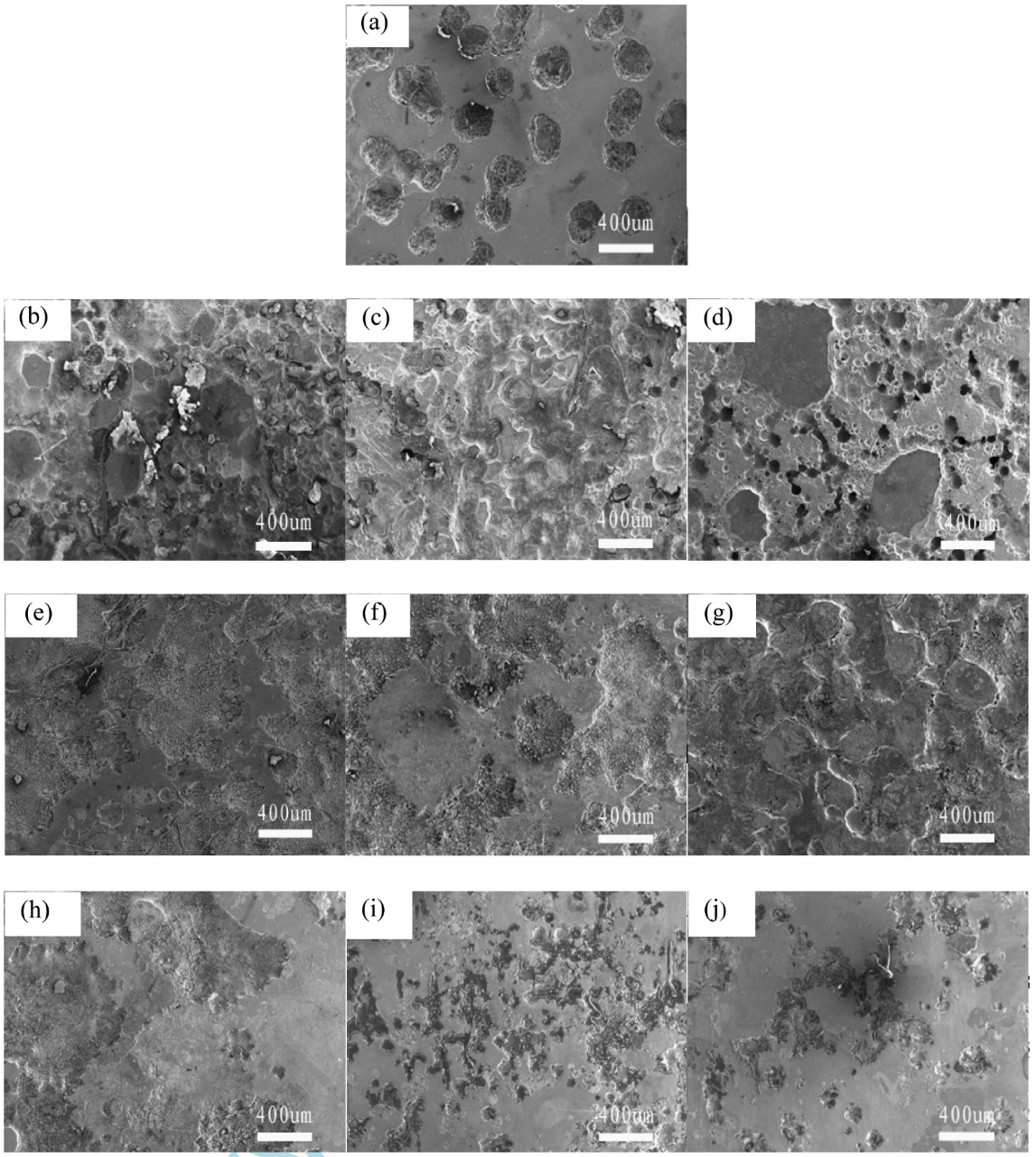


**Figure 5.** Surface morphologies of the specimens after the corrosion test: (a) substrate, (b) 500 °C 1-layer, (c) 500 °C 2-layer, (d) 500 °C 3-layer, (e) 600 °C 1-layer, (f) 600 °C 2-layer, (g) 600 °C 3-layer, (h) 700 °C 1-layer, (i) 700 °C 2-layer, (j) 700 °C 3-layer.

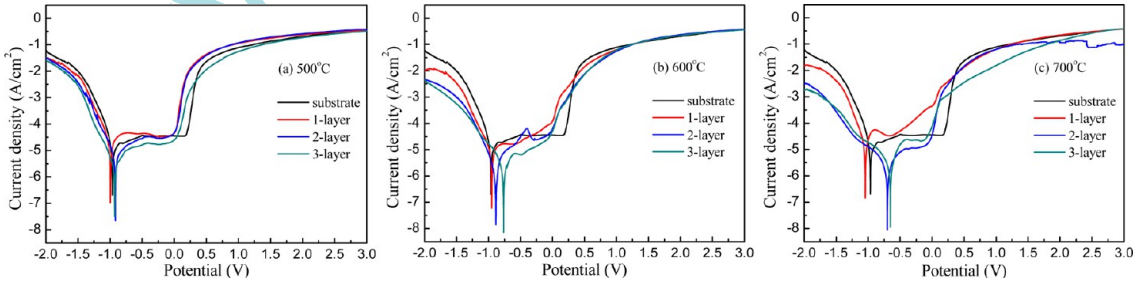


**Figure 6.** Potentiodynamic polarization curves in 5% NaCl for specimens sintering at (a) 500, (b) 600, and (c) 700 °C.

kinetics of $ZrO_2$ crystallites. Compared to the monoclinic phase, the amorphous structure of $ZrO_2$ is more close to the metastable tetragonal phase structure (t′-$ZrO_2$). Therefore, the amorphous $ZrO_2$ in the sintering process gave priority to the formation of t′-$ZrO_2$. However, with the increase of sintering temperature, the $ZrO_2$ molecules got more and more kinetic energy, and the $ZrO_2$ powder was gradually transformed from t′-$ZrO_2$ to m-$ZrO_2$. On the other hand, the grain growth can be


DOI: 10.1021/acsami.5b07915
ACS Appl. Mater. Interfaces 2015, 7, 28264−28272

**Table 2. Corrosion Parameters Estimated from the Potentiodynamic Polarization Curves for Specimens in a 5% NaCl Electrolyte Solution**

| film layer | $E_{corr}$ (V) | log $i_{corr}$ (A/cm$^2$) | $R_p$ (Ω cm$^2$) |
|---|---|---|---|
| substrate | −0.96 | −6.12 | 24 |
| 500 °C 1-layer | −0.99 | −6.84 | 22 |
| 500 °C 2-layer | −0.92 | −7.02 | 59 |
| 500 °C 3-layer | −0.93 | −7.11 | 98 |
| 600 °C 1-layer | −0.95 | −6.63 | 42 |
| 600 °C 2-layer | −0.89 | −7.06 | 190 |
| 600 °C 3-layer | −0.76 | −7.28 | 281 |
| 700 °C 1-layer | −1.04 | −6.16 | 23 |
| 700 °C 2-layer | −0. 69 | −6.84 | 156 |
| 700 °C 3-layer | −0. 65 | −7.16 | 242 |

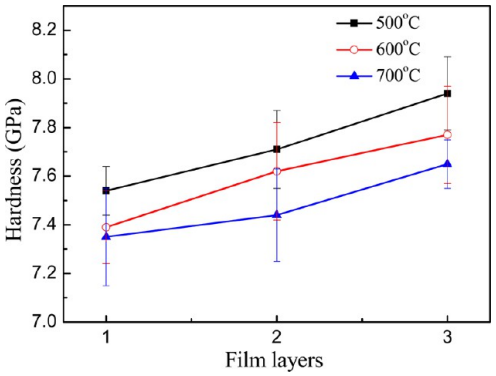


**Figure 7.** Hardness of the $ZrO_2$ films.

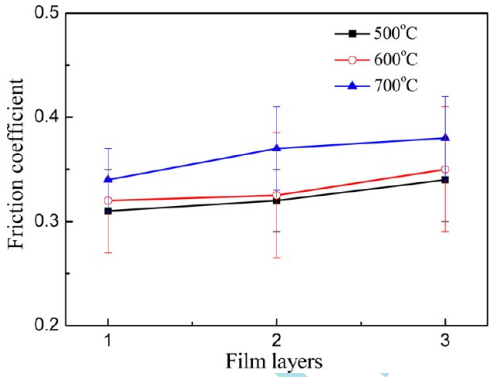


**Figure 9.** Friction coefficient of the $ZrO_2$ films.

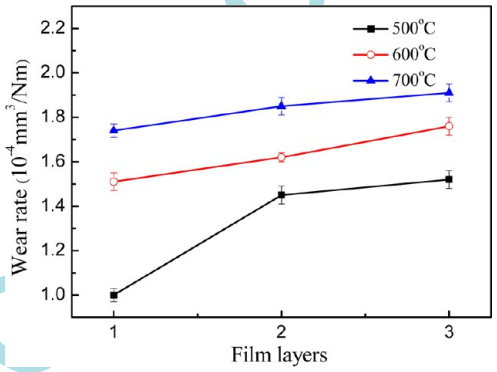


**Figure 10.** Wear rate of specimens.

regarded as the mutual connection between the grains; that is, the grain growth is caused by the mutual contact and connection between the grains so that the grain boundaries are formed, which leads to the disappearance of small grains and the formation of large grains.[31,32]

The thicknesses of the $ZrO_2$ films with one, two, and three layers were approximately 150, 210, and 280 nm, respectively. The results obtained by AFM are displayed in Figure 2. The observed area of the surface was 5 $\mu$m × 5 $\mu$m. The surface morphologies of one, two, and three layers of $ZrO_2$ films which were sintered at 500 °C are shown in Figure 2a−c. It can be observed that the surfaces of the one-layer films are not smooth and there are remarkably large vertical fluctuations which were caused by the polishing scratches on the substrate surface. When the substrate was coated with two layers of $ZrO_2$ films, the surfaces of the specimens became smooth and the grains possessing a cone shape were distributed compactly. With the film thickness increasing, the fluctuations in the height were reduced. When the number of film layers is three, as shown in Figure 2c, the films' surfaces are smoother, the densification of the $ZrO_2$ grains is increased, and the grain size of the cone-shaped particles is decreased.

Figure 2d−f presents the AFM images of the one, two, and three layers of $ZrO_2$ films that were sintered at 600 °C, respectively. In comparison with Figure 2a, the sintering temperature to 600 °C results in an apparent increase of the grain size of the one-layer film and its particles are loosely distributed, as shown in Figure 2d. In addition, the increase in the number of film layers obviously improves the smoothness of the films surface (in Figure 2e,f). With more layers, the grain densification is progressively increased, and the grain size is gradually decreased.

Furthermore, when the sintering temperature rises to 700 °C, the resultant film surface is uneven, as shown in Figure 2g,h; the $ZrO_2$ grains with an ellipsoidal shape are unevenly distributed. However, the surface of the three-layer film is

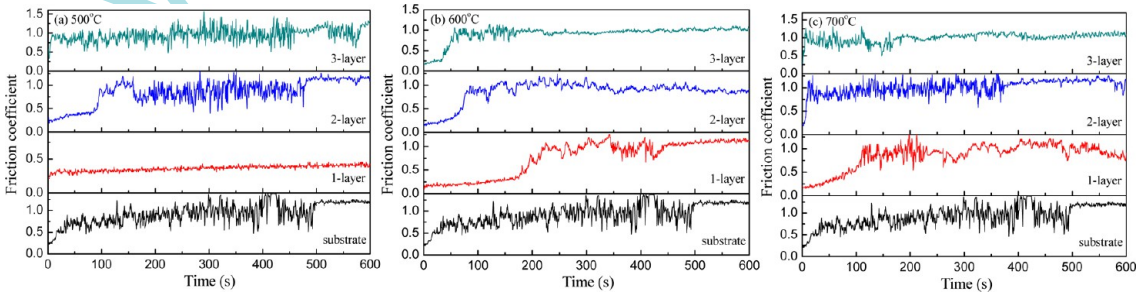


**Figure 8.** Friction coefficient curves of specimens sintered at (a) 500, (b) 600, and (c) 700 °C.



DOI: 10.1021/acsami.5b07915
ACS Appl. Mater. Interfaces 2015, 7, 28264−28272

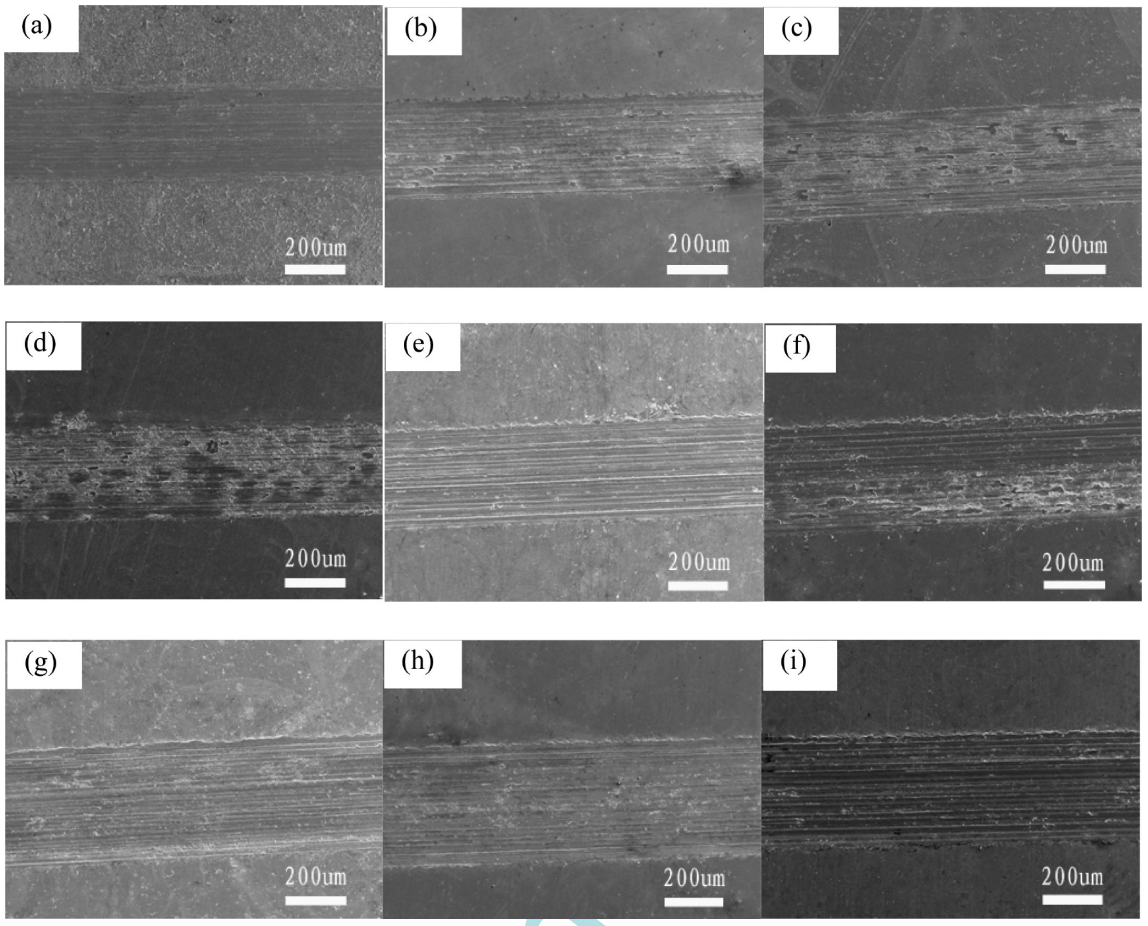


**Figure 11.** Worn morphologies of specimens' surface: (a) 500 °C 1-layer, (b) 500 °C 2-layer, (c) 500 °C 3-layer, (d) 600 °C 1-layer, (e) 600 °C 2-layer, (f) 600 °C 3-layer, (g) 700 °C 1-layer, (h) 700 °C 2-layer, (i) 700 °C 3-layer.

uniform with the reduced grain sizes that are evenly distributed, as shown in Figure 2i.

Figures 3 and 4 show the variations in the average grain size and in the root-mean-square roughness (Sq) of $ZrO_2$ films as a function of the sintering temperature. When combined with the data in Figure 2, it can be observed from Figures 3 and 4 that there is a gradual decrease in the observed grain size and roughness with the number of layers increasing (for a given sintering temperature). However, with increasing sintering temperatures, the grain sizes and surface roughnesses of the $ZrO_2$ films gradually increased. The grain sizes of one-, two- and three-layer $ZrO_2$ films sintered at 500 °C are 53.7, 49.3, and 45.8 nm, and their surface roughnesses are 2.7, 2.6, and 2.5 nm, respectively, whereas the grain sizes of the one, two, and three layers that were sintered at 600 °C are 62.4, 59.1, and 53.6 nm, and the surface roughnesses are 3.8, 3.5, and 3.1 nm, respectively. When the sintering temperature is raised to 700 °C, the grain size of the one-, two-, and three-layer films increases to 80.1, 68.1, and 59.6 nm and the surface roughness increases to 11.8, 11.1, and 4.9 nm, respectively. This is because it was only at the same temperature that the smoothness of the films' surfaces improved with the increase of the number of film layers. Furthermore, the surface grains are better distributed and more compact, which is reflected in the decreased grain size and surface roughness. Nevertheless, the roughness increased with sintering temperature and could be associated with the accretion of grain size, which caused greater differences between the hills and the valleys detected by AFM.[33]

Figure 5 shows the surface morphologies of the specimens after corrosion testing in a NaCl solution. It is observed that the surface of the uncoated stainless steel substrate contains many irregular and deep pits, as shown in Figure 5a. The morphologies of the corroded surface of $ZrO_2$ films with one, two, and three layers that were sintered at 500 °C are displayed in Figure 5b–d. It can be observed that the surfaces of the one-layer films are severely corroded. A large number of film fragments are scattered on the specimen surface. The corrosion of the two-layer film surface is uniform with many small and shallow pits, but deep crevice corrosion exists at the boundaries of the large grains. The damage done to the three-layer film surface is reduced, and the corrosion pits are well distributed. Figure 5e–g shows the morphologies of the corroded surface of $ZrO_2$ films with one, two, and three layers that were sintered at 600 °C. As shown in Figure 5e, the surface corrosion of the one-layer film is serious, and most of the film is corroded into sparsely distributed microparticles. In comparison to the single layer of $ZrO_2$ films, the corrosion area of the two-layer film surface is reduced. Furthermore, only a small portion of the film surface is corroded in the three-layer film (in Figure 5g), and the film's surface is relatively intact except for the crevice corrosion between the large fragments of the film. Compared to the films sintered at 500 and 600 °C, the surface morphology of the films sintered at 700 °C, as shown in Figure 5h–j, displays larger regions that appear not to be affected by corrosion, and the regions of the corroded films decrease with the film thickness increasing. In particular, the surface of the three-layer




DOI: 10.1021/acsami.5b07915
ACS Appl. Mater. Interfaces 2015, 7, 28264–28272

film is nearly the original state. With only a small quantity of shallow corrosion pits, the remaining film surface regions are identical to the film morphology prior to corrosion. These results indicate that the three-layer $ZrO_2$ films sintered at 700 °C exhibit the best corrosion barrier performance compared to other films.

Figure 6 presents the potentiodynamic polarization curves in 5% NaCl for specimens that were sintered at different temperatures. As observed in Figure 6, the current density of the coated specimens in the cathodic polarization region gradually decreases with an increase in the electric potential, which is similar to that of the stainless steel substrate. When the electric potential is greater than −1.0 V, the specimens enter the anode polarization process and the corrosion potentials of the specimens exhibit a positive shift with an increase in the number of film layers. In general, the value of the corrosion potential ($E_{corr}$) can be used to estimate the corrosion tendency of the specimen. At the same time, the corrosion current density (log $i_{corr}$) decreased and the polarization resistance ($R_p$) increased, which implies that the corrosion rate decreases and the corrosion resistance of the specimen increases. Therefore, it is necessary to simultaneously consider the values of $E_{corr}$, log $i_{corr}$, and $R_p$ to evaluate the corrosion performance of the specimen.

The corrosion parameters estimated from the potentiodynamic polarization curves of all of the specimens are summarized in Table 2. It can be observed from the table that the corrosion current density gradually decreases just as the polarization resistance gradually increases with an increase in the sintering temperature and the number of film layers. Combined with the morphological data in Figure 5, it can be concluded that the corrosion resistance of $ZrO_2$ films was gradually improved with increasing sintering temperatures and a greater number of layers (thicker film). The film with three layers, which was sintered at 700 °C, shows excellent corrosion resistance. This is because the quality of the films has an important effect on their corrosion behavior. Structural defects such as cracks, pores, and pinholes in the films could be used as channels for the corrosion of substrate so that the corrosion was far more serious than the films with no defects.[28] Moreover, a higher sintering temperature and more film layers lead to the gradual improvement of the film surface morphology, and higher quality films contribute to the enhancement of corrosion resistance.[34,35]

The hardness of the specimen was determined by nanoindentation tests. The hardness value of the 304 stainless steel substrate is 4.86 GPa, and the hardness of the $ZrO_2$ films is shown in Figure 7. As observed from the figure, the hardness of the films decreases with increasing sintering temperatures. The hardnesses of the one-layer films sintered at 500, 600, and 700 °C are approximately 7.54, 7.39, and 7.35 GPa, respectively. This variation in the hardness values can be associated with the increased grain size and surface roughness, which is observed at high temperatures.[33,36] In addition, with the number of film layers increasing, the hardness value of the film is progressively increasing. The hardness values for two and three layers of $ZrO_2$ films sintered at 500 °C are raised to 7.71 and 7.94 GPa, respectively. This is because the grain size and surface roughness decreased with an increase in film thickness, which is characteristic of film surfaces becoming smoother and more compact.[37]

Figure 8 shows the representative friction coefficient curves of the specimens that were sintered at different temperatures. It can be observed that the friction coefficient of the stainless steel substrate fluctuates around 0.86 while it is sliding against the steel ball, Nevertheless, in the initial stage of sliding, the friction coefficients of the coated specimens clearly decrease, and the fluctuations in the curves are insignificant. This finding indicates that the $ZrO_2$ films can significantly reduce the friction coefficient of the substrate surface. In addition, with a prolonged sliding time, the friction coefficient of the coated specimens abruptly increases and then fluctuates before equalizing at a value near 0.86. This is because the high hardness and low friction coefficient of the $ZrO_2$ films initially resists abrasion by the steel ball. With increasing in sliding time, the films rupture and delaminate under frictional forces. The stripped film fragments become grinding materials that accelerate film failure by rapidly increasing the friction coefficient.[38] Afterward, the $ZrO_2$ films are gradually worn down to the stainless steel substrate, where the friction coefficient is stabilized.

Meanwhile, the wear life of $ZrO_2$ films can be estimated from the duration beginning at the initial contact and ending with the abrupt increase in the friction coefficient. As shown in Figure 8, the friction coefficient of the one-layer film sintered at 500 °C retains a value of approximately 0.31 after contact with the sliding steel ball for 10 min. However, it is readily observed that the wear life of the films reduces with the increase of the number of film layers. This may be due to the fact that the single layer of $ZrO_2$ films covered on the substrate surface closely and uniformly during the dip-coating and sintering process. Nevertheless, when the number of film layers was increased to two or even three layers, the former flat film layer became the deposition surface for the next film. Then, the next film sol covered on the former film's surface and was crystallized in the subsequent sintering process. Because the starting surface is different and the bonding between the film layers is weak, the films become more vulnerable to damage. Furthermore, under repetitive contact with the sliding steel ball, the thermal and contact stresses can lead to fatigue of the interfacial adhesion between the film layers. As a result, brittle fracture and delamination of the films occurred and wear debris was produced. Subsequently, the debris could result in severe abrasiveness on the films.[39]

Figure 9 shows the variation of the average friction coefficient of the $ZrO_2$ films with the sintering temperature and number of the film layers. As observed, the friction coefficient of $ZrO_2$ films is increased with the sintering temperature increasing. This is because the surface roughness and grain size of the $ZrO_2$ films increased with the increase of sintering temperature, and accordingly, the hardness decreased. At the same time, the friction coefficient of $ZrO_2$ films increases with the increase of the number of film layers. This is also because the hardness the $ZrO_2$ films improved with the increasing film layers, and the wear debris was more prone to be produced for multilayer films, which results in a high friction coefficient.[39]

The wear rate of the stainless steel substrate is $1.26 \times 10^{-4}$ $mm^3/Nm$. Meanwhile, the wear rate of the specimens as a function of the sintering temperature and the number of film layers is demonstrated in Figure 10. It is observed that the wear rate of the specimen coated with one layer of $ZrO_2$ films sintered at 500 °C is $1 \times 10^{-4}$ $mm^3/Nm$, which was lower than the substrate's. However, the wear rates of the specimens coated with two- and three-layer films sintered at 500 °C are $1.45 \times 10^{-4}$ and $1.52 \times 10^{-4}$ $mm^3/Nm$, respectively. When the




DOI: 10.1021/acsami.5b07915
ACS Appl. Mater. Interfaces 2015, 7, 28264−28272

sintering temperature increased to 600 and 700 °C, the wear rates of one-, two-, and three-layer films are enhanced by 51%, 18%, 16% and 74%, 28%, 25% compared with those sintered at 500 °C, respectively. These enhanced wear rates were a reflection of the gradual increase in the grain size and the surface roughness with the sintering temperature increase. Moreover, the brittle fracture and delamination was more prone to occur for multilayer films, which produced severe surface fracture, relatively high friction coefficients and material wear rates.[40]

Figure 11 shows the worn surfaces of specimens. It can be observed from Figure 11a that the wear track of the specimen surfaces coated with one layer of the $ZrO_2$ films and sintered at 500 °C is relatively smooth. There are few abrasive particles, and narrow, shallow ploughs are the result of slight scratching. Nevertheless, with the increase of the number of film layers, serious film rupture occurred, which generated many particles and debris such that a wide, deep, and rough wear track is produced. The peeling films produced a scaly plastic deformation belt that shows the features of fatigue wear. Furthermore, as shown in the wear tracks of the specimens after sintering at 600 and 700 °C, fatigue fracture occurred and an even larger number of abrasive particles were generated. The surfaces of these specimens were severely worn, the wear tracks were rough, and much deeper furrows existed there.

## 4. CONCLUSIONS

In summary, we have successfully synthesized the $ZrO_2$ films as a surface modification layer for 304 stainless steel through the sol−gel techniques. The effect of sintering temperature and the number of film layers on the corrosion and tribology properties of the $ZrO_2$ films was discussed in detail. The three-layer films sintered at 700 °C displayed optimal structure characteristics of uniform and dense surface morphology, which significantly enhanced the corrosion resistance of the 304 stainless steel substrate in a 5% NaCl solution at room temperature. Therefore, this $ZrO_2$ film can be applied to a broad range of devices as a protection barrier layer for stainless steel in automotive, household appliances, business machines, and heavy construction such as marine and chemical industries.

With respect to the tribological behavior of the films coated on stainless steel, it was concluded that the wear resistance of the $ZrO_2$ films did not depend on the sintering temperature and the film's thickness. Nevertheless, the one-layer films sintered at 500 °C displayed better tribology properties, which is due to their relatively lower friction coefficient and longer wear life. Consequently, by selecting the suitable sintering temperature and the number of film layers, it will be possible to obtain the $ZrO_2$ films with microstructure and tribology properties optimized to satisfy the requirements of specific applications as protection barriers.

## AUTHOR INFORMATION

### Corresponding Author

*E-mail: jgj@imut.edu.cn.

### Notes

The authors declare no competing financial interest.

## ACKNOWLEDGMENTS

This work was supported by the National Natural Science Foundation of China (11462017) and the Natural Science Foundation of Inner Mongolia Autonomous Region, China (2014BS0104).

## REFERENCES

(1) Li, L.; Dong, C. F.; Xiao, K.; Yao, J. Z.; Li, X. G. Effect of pH on Pitting Corrosion of Stainless Steel Welds in Alkaline Salt Water. Constr. *Build. Mater.* **2014**, *68*, 709−715.

(2) Sui, R. J.; Liu, Y.; Wang, W. Q.; Qu, Y. P.; Su, C. G.; Chang, F. Failure Analysis of Austenitic Stainless Steel Pipes in Amine Liquid Regeneration Unit of a Desulfurizer. *Eng. Failure Anal.* **2015**, *57*, 164−170.

(3) Zhiming, L.; Laimin, S.; Shenjin, Z.; Zhidong, T.; Yazhou, J. Effect of High Energy Shot Peening Pressure on the Stress Corrosion Cracking of the Weld Joint of 304 Austenitic Stainless Steel. *Mater. Sci. Eng., A* **2015**, *637*, 170−174.

(4) Hsu, C.-H.; Huang, K.-H.; Lin, Y.-H. Microstructure and Wear Performance of Arc-deposited Ti−N-O Coatings on AISI 304 Stainless Steel. *Wear* **2013**, *306* (1−2), 97−102.

(5) Ćurković, L.; Ćurković, H. O.; Salopek, S.; Renjo, M. M.; Šegota, S. Enhancement of Corrosion Protection of AISI 304 Stainless Steel by Nanostructured Sol-Gel $TiO_2$ Films. *Corros. Sci.* **2013**, *77*, 176−184.

(6) Xing, X. G.; Han, Z. J.; Wang, H. F.; Lu, P. N. Electrochemical Corrosion Resistance of $CeO_2$-Cr/Ti Coatings on 304 Stainless Steel via Pack Cementation *J. Rare Earths* **2015**, *33* (10), 1122−1128.

(7) Joy, K. Optical and Photoluminescence Properties of Nanostructured $ZrO_2$: Tb Thin Films. *Thin Solid Films* **2014**, *556*, 99−104.

(8) Kato, K.; Saito, T.; Shibayama, S.; Sakashita, M.; Takeuchi, W.; Taoka, N.; Nakatsuka, O.; Zaima, S. Stabilized Formation of Tetragonal $ZrO_2$ Thin Film with High Permittivity. *Thin Solid Films* **2014**, *557*, 192−196.

(9) Ling, X. L.; Liu, X. F.; Wang, G.; Fan, Z. X. Influence of Oxygen Partial Pressure on Laser-Induced Damage Resistance of $ZrO_2$ Films in Vacuum. *Vacuum* **2015**, *119*, 145−150.

(10) Lin, Y. J.; Yu, J. F. Photoluminescent, Morphological and Electrical Properties of $ZrO_2$ and $ZrO_2$: Polyvinyl Alcohol Composite Thin Films. *J. Non-Cryst. Solids* **2015**, *426*, 132−136.

(11) Hong, N. H.; Park, C.-K.; Raghavender, A. T.; Ruyter, A.; Chikoidze, E.; Dumont, Y. High Temperature Ferromagnetism in Cubic Mn-Doped $ZrO_2$ Thin Films. *J. Magn. Magn. Mater.* **2012**, *324* (19), 3013−3016.

(12) Liang, L. R.; Zhou, H.; Wu, G. H.; Mo, Z.; Bao, D. H. Dielectric Properties and Bright Red Emission of $Y^{3+}$/$Eu^{3+}$-Codoped $ZrO_2$ Thin Films Prepared by Chemical Solution Deposition. *Ceram. Int.* **2013**, *39* (2), 1335−1340.

(13) Qin, W.; Nam, C.; Li, H. L.; Szpunar, J. A. Tetragonal Phase Stability in $ZrO_2$ Film Formed on Zirconium Alloys and Its Effects on Corrosion Resistance. *Acta Mater.* **2007**, *55* (5), 1695−1701.

(14) Yeh, T.-K.; Chien, Y.-C.; Wang, B.-Y.; Tsai, C.-H. Electrochemical Characteristics of Zirconium Oxide Treated Type 304 Stainless Steels of Different Surface Oxide Structures in High Temperature Water. *Corros. Sci.* **2008**, *50* (8), 2327−2337.

(15) Mi, Y. J.; Wang, J. Q.; Yang, Z. G.; Wang, H. G.; Wang, Z. F.; Yang, S. R. Preparation and Property of $ZrO_2$/Go Multi-Layered Nanocomposite Lubricating Film. *RSC Adv.* **2014**, *4*, 39743−39750.

(16) Benea, L.; Ponthiaux, P.; Wenger, F. Co-$ZrO_2$ Electrodeposited Composite Coatings Exhibiting Improved Micro Hardness and Corrosion Behavior in Simulating Body Fluid Solution. *Surf. Coat. Technol.* **2011**, *205* (23−24), 5379−5386.

(17) Norouzi, M.; Garekani, A. A. Corrosion Protection by Zirconia-based Thin Films Deposited by a Sol Gel Spin Coating Method. *Ceram. Int.* **2014**, *40* (2), 2857−2861.

(18) Cubillos, G. I.; Bethencourt, M.; Olaya, J. J. Corrosion Resistance of Zirconium Oxynitride Coatings Deposited via DC Unbalanced Magnetron Sputtering and Spray Pyrolysis-Nitriding. *Appl. Surf. Sci.* **2015**, *327*, 288−295.

(19) Panicaud, B.; Grosseau-Poussard, J.-L.; Retraint, D.; Guerain, M.; Li, L. On the Mechanical Effects of a Nanocrystallisation Treatment for $ZrO_2$ Oxide Films Growing on a Zirconium Alloy. *Corros. Sci.* **2013**, *68*, 263−274.





DOI: 10.1021/acsami.5b07915
*ACS Appl. Mater. Interfaces* 2015, 7, 28264−28272

(20) Wang, J. Q.; Liu, X. H.; Ren, S. L.; Guan, F.; Yang, S. R. Mechanical Properties and Tribological Behavior of $ZrO_2$ Thin Films Deposited on Sulfonated Self-Assembled Monolayer of 3-Mercaptopropyl Trimethoxysilane. *Tribol. Lett.* **2005**, *18* (4), 429−436.
(21) Obadele, B. A.; Lepule, M. L.; Andrews, A.; Olubambi, P. A. Tribocorrosion Characteristics of Laser Deposited Ti-Ni-$ZrO_2$ Composite Coatings on AISI 316 Stainless Steel. *Tribol. Int.* **2014**, *78*, 160−167.
(22) Ito, A.; You, Y.; Ichikawa, T.; Tsuda, K.; Goto, T. Preparation of $Al_2O_3$-$ZrO_2$ Nanocomposite Films by Laser Chemical Vapour Deposition. *J. Eur. Ceram. Soc.* **2014**, *34* (1), 155−159.
(23) Yin, B.; Liu, G.; Zhou, H. D.; Chen, J. M.; Yan, F. Y. Microstructures and Properties of Plasma Sprayed FeAl/$CeO_2$/$ZrO_2$ Nano-Composite Coating. *Appl. Surf. Sci.* **2010**, *256* (13), 4176−4184.
(24) Li, N.; Suzuki, M.; Abe, Y.; Kawamura, M.; Sasaki, K.; Itoh, H.; Suzuki, T. Effects of Substrate Temperature on the Ion Conductivity of Hydrated $ZrO_2$ Thin Films Prepared by Reactive Sputtering in $H_2O$ Atmosphere. *Sol. Energy Mater. Sol. Cells* **2012**, *99*, 160−165.
(25) Shen, Y. M.; Shao, S. Y.; Yu, H.; Fan, Z. X.; He, H. B.; Shao, J. D. Influences of Oxygen Partial Pressure on Structure and Related Properties of $ZrO_2$ Thin Films Prepared by Electron Beam Evaporation Deposition. *Appl. Surf. Sci.* **2007**, *254* (2), 552−556.
(26) Balakrishnan, G.; Sairam, T. N.; Reddy, V. R.; Kuppusami, P.; Song, J. Microstructure and Optical Properties of $Al_2O_3$/$ZrO_2$ Nano Multilayer Thin Films Prepared by Pulsed Laser Deposition. *Mater. Chem. Phys.* **2013**, *140* (1), 60−65.
(27) Liu, W. M.; Chen, Y. X.; Ye, C. F.; Zhang, P. Y. Preparation and Characterization of Doped Sol-Gel Zirconia Films. *Ceram. Int.* **2002**, *28* (4), 349−354.
(28) Nouri, E.; Shahmiri, M.; Rezaie, H. R.; Talayian, F. Investigation of Structural Evolution and Electrochemical Behaviour of Zirconia Thin Films on the 316L Stainless Steel Substrate Formed via Sol-Gel Process. *Surf. Coat. Technol.* **2011**, *205* (21−22), 5109−5115.
(29) Tiwari, S. K.; Adhikary, J.; Singh, T. B.; Singh, R. Preparation and Characterization of Sol-Gel Derived Yttria Doped Zirconia Coatings on AISI 316L. *Thin Solid Films* **2009**, *517* (16), 4502−4508.
(30) Kumar, S.; Bhunia, S.; Ojha, A. K. Effect of Calcination Temperature on Phase Transformation, Structural and Optical Properties of Sol-Gel Derived $ZrO_2$ Nanostructures. *Phys. E* **2015**, *66*, 74−80.
(31) Lin, Y. C.; Gan, D. S.; Shen, P. Y. Phase Transformation of $ZrO_2$ in MnZn-Ferrite under Magnetic Field. *J. Am. Ceram. Soc.* **1996**, *79* (2), 559−561.
(32) Garvie, R. C.; Goss, M. F. Intrinsic Size Dependence of the Phase Transformation Temperature in Zirconia Microcrystals. *J. Mater. Sci.* **1986**, *21* (4), 1253−1257.
(33) Diaz-Parralejo, A.; Ortiz, A. L.; Caruso, R. Effect of Sintering Temperature on the Microstructure and Mechanical Properties of $ZrO_2$-3 mol% $Y_2O_3$ Sol-Gel Films. *Ceram. Int.* **2010**, *36* (8), 2281−2286.
(34) Di Maggio, R.; Rossi, S.; Fedrizzi, L.; Scardi, P. $ZrO_2$-$CeO_2$ Films as Protective Coatings against Dry and Wet Corrosion of Metallic Alloys. *Surf. Coat. Technol.* **1997**, *89* (3), 292−298.
(35) Sandhyarani, M.; Rameshbabu, N.; Venkateswarlu, K.; Sreekanth, D.; Subrahmanyam, C. Surface Morphology, Corrosion Resistance and In Vitro Bioactivity of P Containing $ZrO_2$ Films Formed on Zr by Plasma Electrolytic Oxidation. *J. Alloys Compd.* **2013**, *553*, 324−332.
(36) Lima, R. S.; Kucuk, A.; Berndt, C. C. Evaluation of microhardness and elastic modulus of thermally sprayed nanostructured zirconia coatings. *Surf. Coat. Technol.* **2001**, *135* (2−3), 166−172.
(37) Paterson, M. J.; Paterson, P. J. K.; Ben-Nissan, B. The Dependence of Structural and Mechanical Properties on Film Thickness in Sol-Gel Zirconia Films. *J. Mater. Res.* **1998**, *13* (02), 388−395.
(38) Ji, G. J.; Shi, Z. M.; Zhang, W.; Zhao, G. Tribological Properties of Titania Nanofilms Coated on Glass Surface by the Sol-Gel Method. *Ceram. Int.* **2014**, *40* (3), 4655−4662.
(39) Ouyang, J. H.; Sasaki, S.; Umeda, K. The Friction and Wear Characteristics of Low-Pressure Plasma-Sprayed $ZrO_2$-$BaCrO_4$ Composite Coating at Elevated Temperatures. *Surf. Coat. Technol.* **2002**, *154* (2−3), 131−139.
(40) Liang, B.; Zhang, G.; Liao, H. L.; Coddet, C.; Ding, C. X. Friction and Wear Behavior of $ZrO_2$-$Al_2O_3$ Composite Coatings Deposited by Air Plasma Spraying: Correlation with Physical and Mechanical Properties. *Surf. Coat. Technol.* **2009**, *203* (20−21), 3235−3242.




DOI: 10.1021/acsami.5b07915
*ACS Appl. Mater. Interfaces* 2015, 7, 28264−28272